Available online at www.sciencedirect.com

Trans. Nonferrous Met. Soc. China 33(2023) 422−437

Transactions of
Nonferrous Metals
Society of China

www.tnmsc.cn

Microstructure evolution, strengthening mechanisms and deformation behavior of high-ductility Mg−3Zn−1Y−1Mn alloy at different extrusion temperatures

Xiao-feng WU, Chun-xiang XU, Zheng-wei ZHANG, Wen-fu YANG, Jing-shan ZHANG

College of Materials Science and Engineering, Taiyuan University of Technology, Taiyuan 030024, China

Received 30 June 2021; accepted 25 March 2022

Abstract: Hot extrusion was performed on as-cast Mg−3Zn−1Y−1Mn alloy to further improve the mechanical properties and investigate its microstructure evolution and deformation mechanism at different thermal deformation temperatures. The experimental results suggested that the alloy at the extrusion temperature of 330 °C had the optimal mechanical properties, and the tensile strength and elongation of the alloy were 270 MPa and 16.8%, respectively. The strength improvement of the as-extruded alloy primarily arose from three aspects, including fine-grain strengthening due to dynamic re-crystallization (DRX), dislocation strengthening not offset by DRX, and second phase strengthening. Continuous dynamic re-crystallization (CDRX) and dynamic recovery (DRV) occurred simultaneously at the extrusion temperature of 300 °C. The discontinuous dynamic re-crystallization (DDRX) occurred at the extrusion temperature of 330 and 360 °C. However, the contribution of {0001} basal plane slip, $\{10\bar{1}0\}$ prismatic type I and $\{11\bar{2}0\}$ prismatic type II slips to plastic deformation was significantly affected by the extrusion temperature. The $\{11\bar{2}0\}$ prismatic type II slip was found to be the most difficult one to initiate among the three slip systems.

Key words: Mg−3Zn−1Y−1Mn alloy; microstructure; deformation mechanism; hot extrusion; dynamic re-crystallization; mechanical properties

---

1 Introduction

Magnesium alloys have aroused rising attention because of their light mass and green degradability. However, the lower strength and poor workability have still been found as two vital factors restricting the large-scale commercial applications of magnesium alloy. Thus, the strengthening and toughening of magnesium alloys have been recognized as an eternal theme in the field of magnesium alloy [1−3]. Heat treatment strengthening primarily consists of adjusting second phase distribution of as-cast alloy to improve the mechanical properties of the alloy. However, heat treatment has a very limited effect on improving the mechanical properties of magnesium alloy. In some circumstances in which the solid solution temperature of Mg−6Zn−3Y−0.5Zr alloy was nearly 350 °C, the crystal grains would grow up rapidly, thus leading to the reduction of mechanical properties of the alloy [4,5].

However, hot extrusion can be conducive to improving the mechanical properties of magnesium alloys. XU et al [6] reported that as-extruded Mg−5.5Zn−1.1Y−0.8Zr (wt.%) alloy containing *I* phase exhibited tensile strength of σ_b=345 MPa, $\sigma_{0.2}$=200 MPa, as well as elongation of 10.8%. The as-cast alloy grains will be greatly refined as DRX and DRV will occur during hot extrusion. Fine grain strengthening has been considered an effective way of strengthening and toughening magnesium alloy, and it can improve the strength and hardness of magnesium alloys, while improving the ductility

---

Corresponding author: Chun-xiang XU, E-mail: xuchunxiang2012@126.com

DOI: 10.1016/S1003-6326(22)66117-X

and toughness of the materials [7]. Thus, fine the grain strengthening outperforms other strengthening methods. Numerous studies have been conducted on the DRX behavior of magnesium alloys during the hot deformation [8−11], and many DRX models have been proposed, which generally consider that the DRX of magnesium alloys during hot extrusion deformation is significantly correlated with the migration of dislocations and grain boundaries. In this study, EBSD was used to observe the migration of dislocation and grain boundary, investigate the changes of stress in the microstructure and dislocation density during the deformation, and systematically clarify the microstructure evolution mechanism of these alloys during thermal deformation.

Besides, the plastic deformation mechanism is highly complicated, and thermal deformation at different temperatures is dependent on the sliding of the base plane and the prismatic plane systems to complete deformation, which largely consist of $\{0001\}$ basal plane slip, $\{10\bar{1}0\}$ prismatic type I and $\{11\bar{2}0\}$ prismatic type II slips. The deformation temperature has been found to be a vital factor for the motivation of different slip systems in magnesium alloys. Relevant research has suggested that both the basal plane slip and prismatic slip systems in magnesium alloys are $\langle a\rangle$ slips [9,10]. The sliding direction of the $\{0001\}$ basal plane slip is parallel to the basal plane while it is perpendicular to the c axis, besides the sliding direction of the $\{10\bar{1}0\}$ prismatic type I consists of the $\langle 0001\rangle$ direction parallel to the c axis and the $\langle 0001\rangle$ direction perpendicular to the c-axis $\langle 1120\rangle$ direction, and the sliding direction of the $\{11\bar{2}0\}$ prismatic type II slip refers to the $\langle 0001\rangle$ direction parallel to the base plane [10,11]. The pyramidal slip system is the most difficult to start. The critical shear stress of the pyramidal sliding plane at ambient temperature is nearly two magnitude orders higher than that of the basal plane slip system, and one magnitude order higher than that of the prismatic slip system [12]. Accordingly, the pyramidal slip system is more difficult to start than the basal slip and prismatic slip systems. However, the pyramidal slip system is capable of providing 5 independent slip systems. In particular, slip direction $\langle\bar{1}\bar{1}23\rangle$ can effectively coordinate deformation along the c-axis direction, and the von-Mises yield criterion is satisfied even if the basal and prismatic slip systems cannot be activated at higher temperatures [13−16].

In this study, hot extrusion was used to improve the mechanical properties of the as-cast Mg−3Zn−1Y−1Mn alloy, and the evolution of microstructure and deformation mechanism at different extrusion temperatures were illustrated using electron backscatter diffraction (EBSD), which laid a theoretical foundation for further research.

2 Experimental

The experimental materials consisted of high purity magnesium ingot (99.5%), zinc (Zn) (99.99%), yttrium (Y) (99.99%) and manganese (Mn) (99.99%). The smelting experiment was performed using a high-frequency resistance furnace. The mixed gas (99% CO_2 and 1% SF_6) was adopted to prevent magnesium melting oxidation. After all the alloying elements were added completely, the liquid magnesium alloy was hold for 30 min and then poured into a d20 mm × 18 mm cylindrical cast iron mold. Subsequently, homogenization treatment should be performed for the as-cast magnesium ingot before the ingot was extruded, and then the ingot was placed in a resistance furnace at 300 °C for 12 h.

After the homogenization heat treatment was performed, the magnesium ingot was placed in an extrusion die at an extrusion ratio of 16:1, as presented in Fig. 1. The extrusion rate was 60 mm/min, and the extrusion temperature was 300, 330 and 360 °C, respectively. Finally, an extruded rod with a diameter of 10 mm was obtained.

The mechanical properties were ambient-temperature tensile properties, using the DNS100 electronic universal testing machine. The standard sample was prepared with DK7720 wire EDM. We conducted four sets of tensile experiments at each extrusion temperature and took the average value. The microscopic observation was conducted by optical microscope LeicaDM2500M. The fracture morphology was characterized by scanning electron microscope (SEM, MIRA3-TESCAN). The phase composition was characterized by the energy spectrometer (EDS), and Y−2000 X-ray diffractometer (XRD). The sample used in EBSD experiment was a small cube of 5 mm × 4 mm × 4 mm, the voltage of the DC power supply was

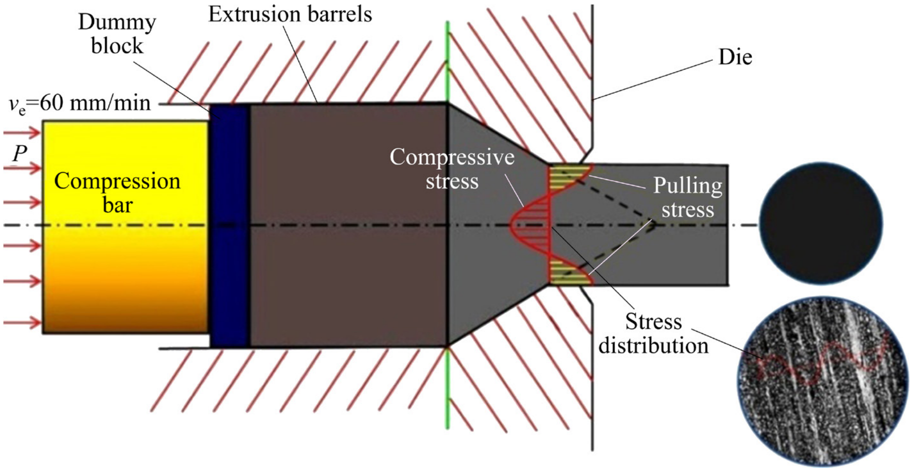

Fig. 1 Extrusion schematic diagram and stress distribution at die hole

controlled at 15−20 V, the current was controlled at 0.1−0.5 A, and the electrolysis time was 120−200 s. The nano-mechanical properties, including micro-hardness and elastic modulus, were measured by Nano Indenter G200 as the average of 10 values.

3 Results

3.1 Microstructure evolution during extrusion

Figure 2 presents the metallographic micrographs of the as-cast alloy as well as different as-extruded alloys, and the corresponding grain size distribution at different extrusion temperatures. The XRD pattern of Fig. 3 suggests that the black located at grain boundary of the as-cast alloy was quasi-crystal *I* phase, which was dispersed and distributed on the α-Mg matrix in cluster form. The as-cast microstructure was significantly refined after extrusion.

The DRXed grains accounted for nearly 62.5% at 300 °C, and the average grain size of DRXed grains (d_m) was 2.25 μm. The DRXed grain proportion increased to 89.6% at 330 °C. However, DRXed grain size increased slightly, the average grain size was 3.12 μm, and most of the grains were concentrated between 2.5 and 5 μm, even there were a few grains much larger than 16 μm. The un-DRXed grains were elongated along the extrusion direction. In this type of microstructure the coexisted DRXed and un-DRXed grains constituted a typical "bimodal structure" [17,18]. The research by MIRZA et al [14] showed that "bimodal structure" endowed alloys with good comprehensive mechanical properties. The DRXed grains provided ductility for the alloy, while the un-DRXed grains ensured the strength. With the temperature increasing to 360 °C, the DRX proportion and average grain size further increased to 92.7% and 4.29 μm, respectively.

3.2 Texture characteristics of as-extruded Mg−3Zn−1Y−1Mn alloy at different extrusion temperatures

EBSD orientation maps, grain size distribution and statistics at different extrusion temperatures are presented in Fig. 4. Different grain colors in SF diagram represent different grain orientations. Figure 4 suggests that the crystal orientation of the un-DRXed region was between the $\langle 0001\rangle$ crystal direction and the $\langle \bar{1}2\bar{1}0\rangle$ crystal direction, while the orientation of DRXed grains was primarily $\langle 01\bar{1}0\rangle$. The crystal orientation $\langle 0001\rangle$ of the red un-DRXed grain is parallel to the *c* axis, which was a typical as-extruded alloy wire texture [19]. In general, the grain boundary of the orientation difference between adjacent grains less than 15° was termed as low-angle grain boundaries (LAGBs), and the orientation difference higher than 15° was termed as high angle grain boundaries (HAGBs) [20]. According to the grain orientation distribution diagram, most grain orientations were concentrated at 2°−20°, in particular, 2°−8° accounted for a large proportion. As revealed by HAGBs and LAGBs distribution diagrams (Figs. 4(b, d, f)), the green LAGBs were mainly concentrated in un-DRXed area, while black HAGBs were concentrated in DRXed grains. Moreover, as the extrusion temperature increased,

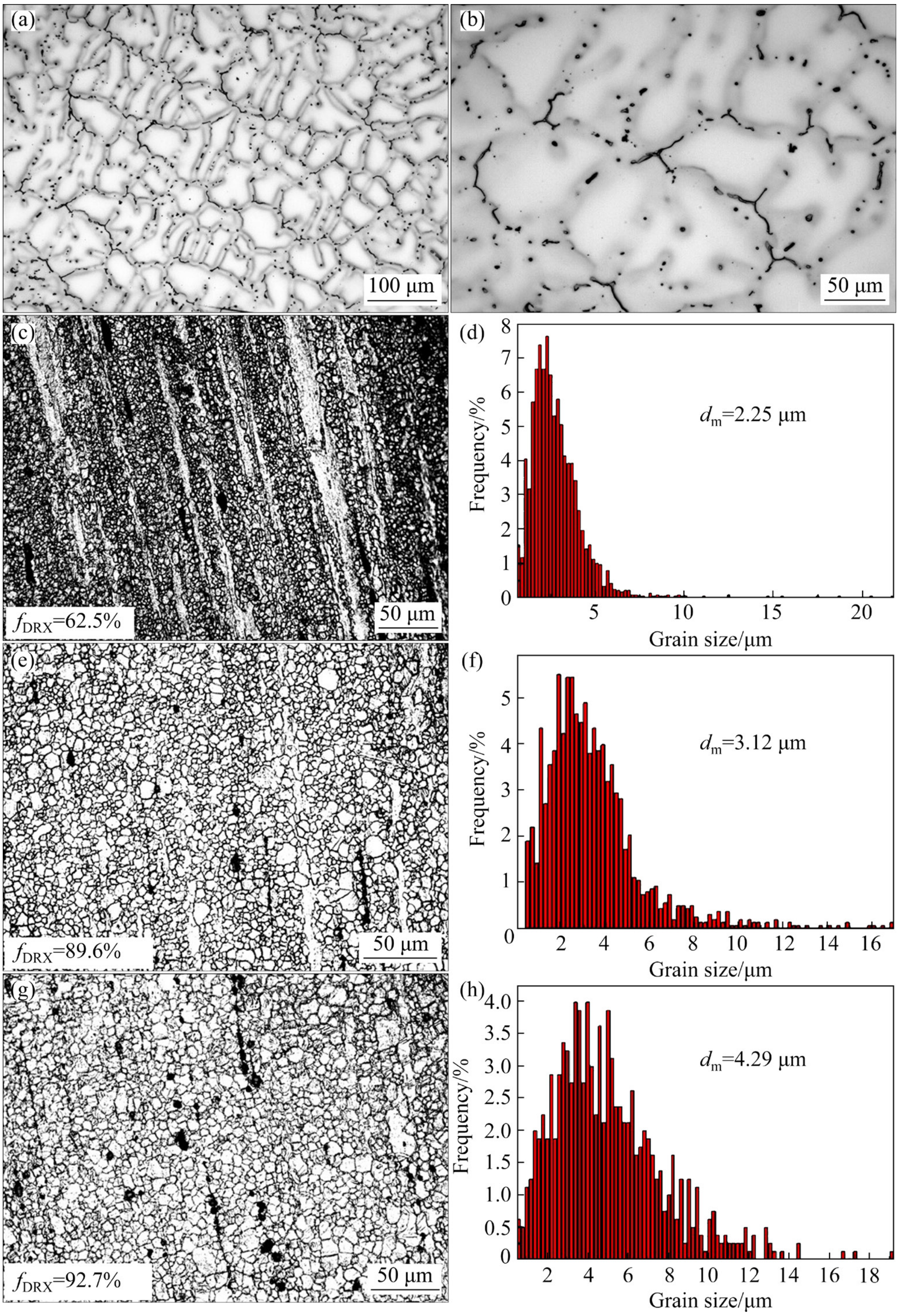

Fig. 2 Metallographic micrographs and corresponding grain size distribution of as-cast and as-extruded alloys at different temperatures: (a, b) As-cast; (c, d) 300 °C; (e, f) 330 °C; (g, h) 360 °C

the green LAGBs proportion tended to decrease, while the proportion of black HAGBs increased. Statistics suggests that green LAGBs proportions at different extrusion temperatures accounted for 58% (300 °C), 49% (330 °C) and 37% (360 °C), respectively.

Figure 5 shows EBSD pole diagrams and Schmid factor (m_s) statistics on different slip planes. The {0001} basal plane exhibits a typical fiber texture parallel to the ED direction at the extrusion temperature of 300 °C. The maximum texture intensity appearing on the $\{10\bar{1}0\}$ prismatic type I plane was 17.14. The m_s values on the $\{11\bar{2}0\}$ prismatic type II and $\{10\bar{1}0\}$ prismatic

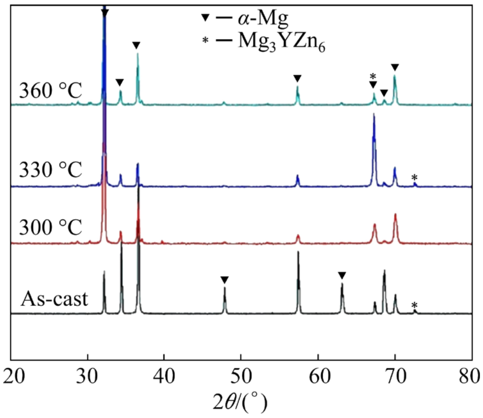

Fig. 3 XRD patterns of as-cast and as-extruded alloys at different extrusion temperatures

type *I* planes were significantly greater than that on the {0001} basal plane. With the extrusion temperature increasing to 330 °C, the maximum texture intensity appeared on the {0001} basal plane and decreased to 12.45. However, the texture on the {0001} basal plane parallel to the ED direction inclined to the TD direction. Some research results showed that ideal fiber texture was basal fiber texture $\langle 10\bar{1}0\rangle$//ED [7,21], but the non-basal slip system starting would cause the basal plane texture to be inclined to TD direction due to the increased deformation temperature. However, Schmidt factor on different slip systems has a significant relationship with the *c*/*a* lattice constant

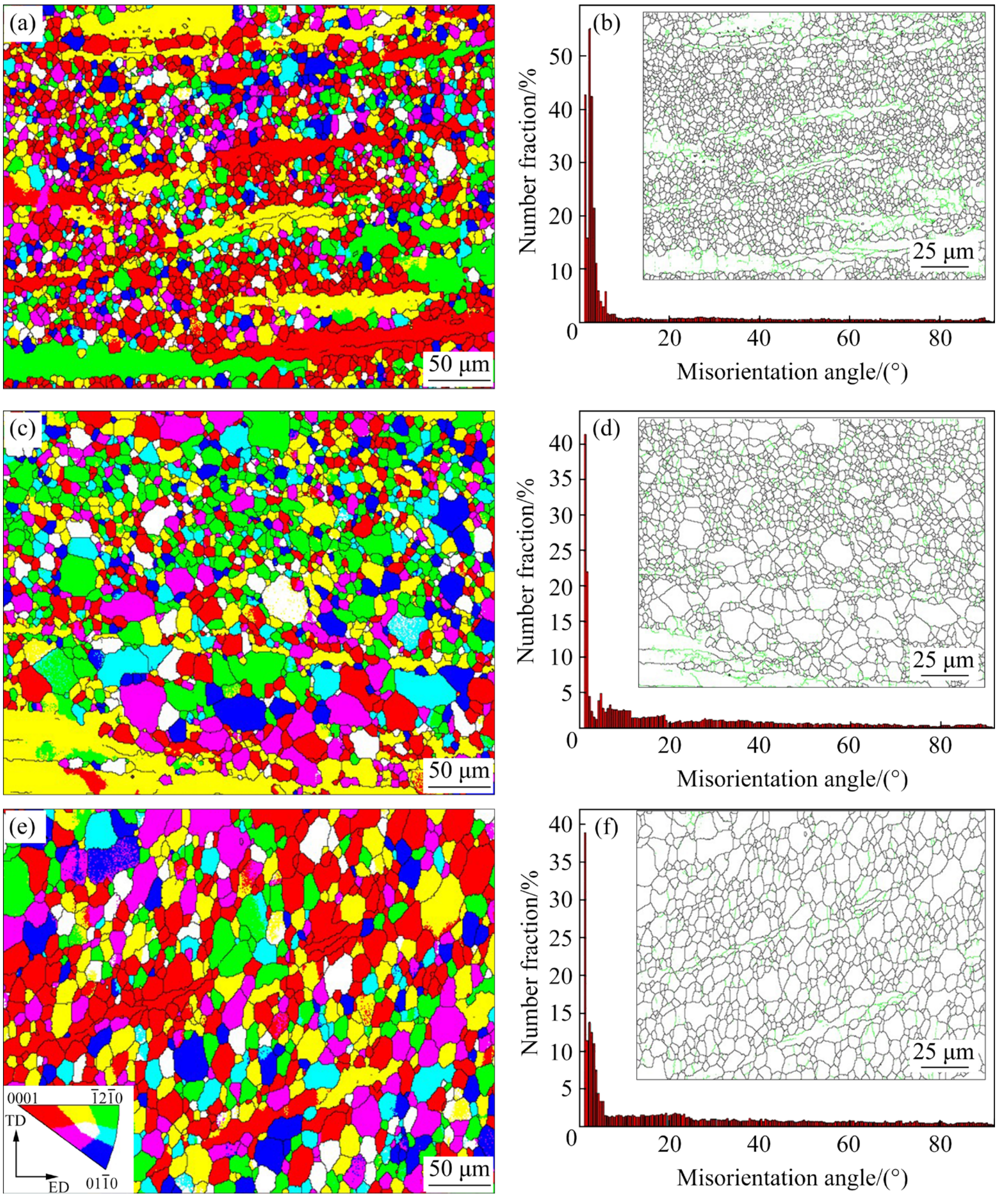

Fig. 4 EBSD orientation maps (a, c, e), misorientation angle distribution and grain boundary figures (b, d, f) (black is high-angle boundary and green is low-angle boundary) of alloys extruded at different temperatures: (a, b) 300 °C; (c, d) 330 °C; (e, f) 360 °C

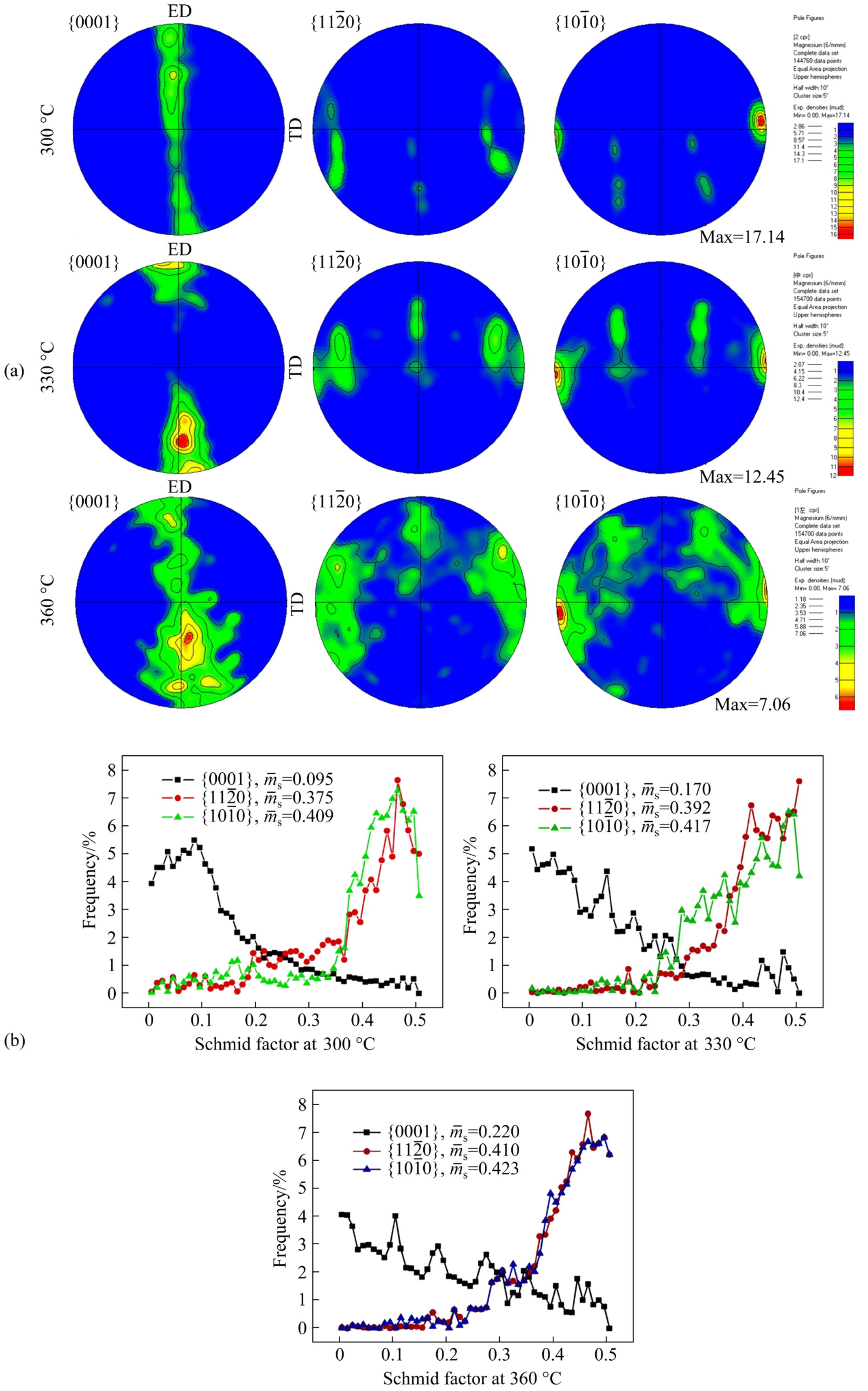

Fig. 5 EBSD pole diagrams (a) and average Schmid factor values ($\bar{m}_s$) (b) of as-extruded alloy on different slip planes at different extrusion temperatures

ratio. The research of LIU et al [15] showed that atomic radius difference between the RE and Mg elements would reduce the *c*/*a* lattice constant ratio, which could be beneficial to the non-basal plane slip system starting. With the increase in the extrusion temperature to 360 °C, the texture of the {0001} basal plane was clearly at an angle to the ED direction, and the texture intensity on the $\{10\bar{1}0\}$ and {1120} prismatic planes was further enhanced. The value of m_s on each slip system also increased further. The maximum texture intensity decreased to 7.06.

3.3 Mechanical properties of as-extruded Mg−3Zn−1Y−1Mn alloy

To better analyze the deformation behavior during extrusion process, the engineering stress−engineering strain curve was converted into the true stress−true strain curve. The conversion process is expressed as follows [22]:

$$\varepsilon_{\mathrm{T}}=\ln\frac{H_0}{H} \tag{1}$$

where ε_{T} is the true strain, H_0 and H denote the heights of the sample before and after compression, respectively, and the true stress during compression (σ_{T}) is calculated by the following equation:

$$\sigma_{\mathrm{T}}=\frac{P}{S}=\frac{P}{S_0\mathrm{e}^{\varepsilon}} \tag{2}$$

where P denotes the axial load, S_0 and S represent the cross-sectional areas of the specimen before and after compression, respectively, and ε is the strain. Figure 6(a) shows the true stress−true strain curves of the ingot at three extrusion temperatures. All curves contained three stages. At the first stage, the dislocation density inside the deformed grains increased sharply due to the deformation, thus leading to work hardening and the increase of stress. However, the increase of dislocation density at the second stage stimulated DRX or DRV. Subsequently, the softening effect of DRX or DRV was greater than work hardening, and the stress began to decrease. The third stage entered a stable flow stage. Since magnesium alloys had low stock fault energy, DRV was prone to occur at lower temperatures, while DRX would occur at high temperatures. The research results of NAN et al [23] revealed that there was no obvious weakening to the peak stress in DRV which involves dislocation density increasing. As indicated by the true stress−true strain curve at 300 °C, it would directly enter into the stable rheological state. However, the stress peak would decrease to stable flow stress during the crystallization [24]. The research results of JIANG et al [25] revealed that the difference between the peak stress (σ_1) and the steady-state flow stress (σ_2) represents the softening degree during hot deformation. Accordingly, with the increase in the extrusion temperature, as shown in Fig. 6(b), the difference between the peak stress (σ_1) and the steady-state flow stress (σ_2) tended to increase.

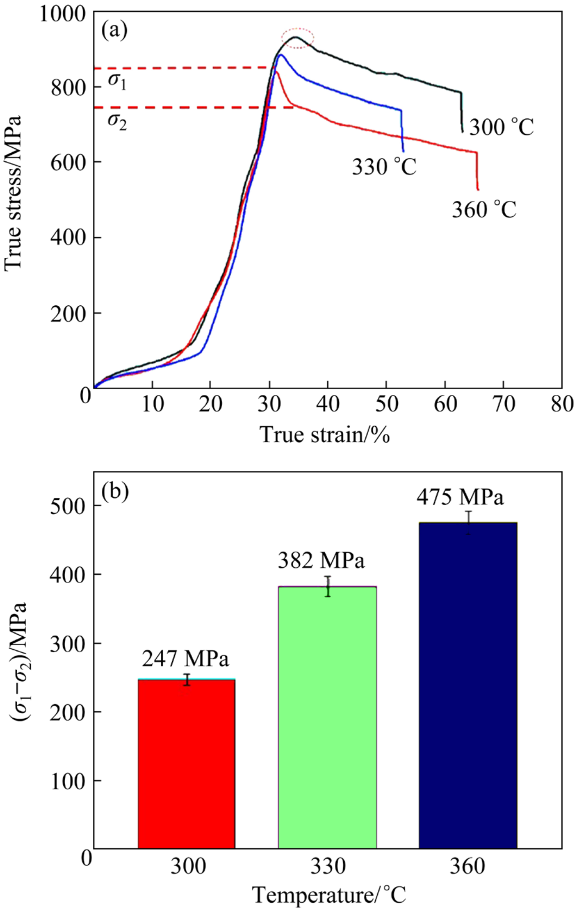

Fig. 6 Compressive true stress−true strain curves of ingot at different temperatures (a) and difference between peak stress (σ_1) and steady-state flow stress (σ_2) (b)

Figure 7 and Table 1 show the tensile stress−strain curves and mechanical properties of as-cast and as-extruded alloys. It is found that the as-cast alloy exhibited good ductility at ambient temperature, and its elongation reaches 20%, its yield strength and ultimate tensile strength were 76 and 189 MPa, respectively. The 300 °C as-extruded alloy had the highest strength, and its ultimate tensile strength and elongation were 287 MPa and 10.5%, respectively. The comprehensive mechanical properties of the specimen at 330 °C were optimal, its yield strength, ultimate tensile strength and elongation reached 203 MPa, 268 MPa and 16.8%, respectively. Good comprehensive mechanical properties benefited from the "bimodal structure" that composed of large-sized grains and small-sized grains [14]. Compared with those of the as-cast alloy, the mechanical properties of as-extruded alloys have been significantly improved.

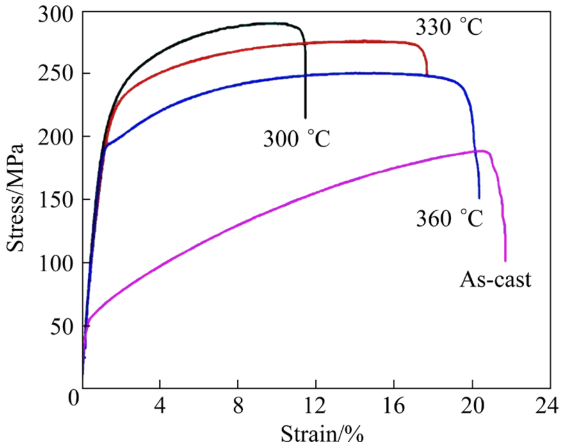

Fig. 7 Tensile stress−strain curves of as-cast and as-extruded alloys

Table 1 Mechanical properties of as-cast and as-extruded alloys

Specimen	Ultimate tensile strength/MPa	Yield strength/MPa	Elongation/%
As-cast	189±0.9	76±0.4	20.1±0.2
Extruded at 300 °C	287±3	230±3	10.5±0.7
Extruded at 330 °C	268±3	203±3	16.8±1.2
Extruded at 360 °C	243±3	177±2	19.6±1.2

Since there was friction between the bar surface and abrasive tool, as shown in Fig. 1, bar surface was affected by pulled stress while the core was squeezed and was affected by compressive stress. The stress distribution was similar to a cosine curve [26], thus constituting the main source of macroscopic residual stress. Besides, the deformation between the grains and sub-grains was not uniform, a considerable number of dislocations and vacancies inside the metal led to lattice distortion in microscopic crystal, thus constituting the main source of microscopic residual stress. The DRX softening effect largely offsets the residual stress caused by plastic deformation [27]. However, the DRX proportion could not reach 100%, and considerable amount of residual stress remained. The presence of residual stress significantly affected mechanical properties of alloy. Figures 8(a−c) show the EBSD stress contour maps of different as-extruded alloys. The statistical result in Figure 8(d) demonstrated that the residual stress at 300 °C was the largest, but that at 360 °C was the smallest. This is because the high dynamic recrystallization proportion at higher temperatures reduced work hardening and decreased the residual internal stress.

4 Discussion

4.1 Effect of extrusion temperature on DRX mechanism

The thermoplastic deformation would cause DRV, CDRX and DDRX inside deformed grains to offset the work hardening and reduce the dislocation density. The softening mechanism also changed with different deformation temperatures.

Figure 9 shows kernel average misorientation (KAM) graphs and LocMis statistics, both of which represent uniformity degree of plastic deformation and dislocation density level. The color changes from blue to green represent the dislocation density difference. LocMis figure shows orientation difference between any data point within the respective grain and adjacent data points in the EBSD area scan data. LocMis is highly sensitive to small changes in the grain orientation. Then, we can use LocMis to study the orientation change within the deformed grain [28]. As revealed by the research of YAN et al [29] that the average LocMis value is positively correlated with the dislocation density, and the higher the dislocation density is, the larger the average LocMis value will be. The relationship between dislocation density (ρ^{GND}) and the average LocMis value is expressed as [26]

$$\rho^{\mathrm{GND}}=2\mathrm{KAM}_{\mathrm{av}}/(\mu b) \tag{3}$$

where μ denotes the step size, b represents the magnitude of the Burgers vector, and $\mathrm{KAM}_{\mathrm{av}}$ represents the average KAM value of the selected area, which can be calculated by

$$\mathrm{KAM}_{\mathrm{av}}=\exp\left[\frac{1}{N}\sum_{1}^{i}\ln \mathrm{KAM}_{\mathrm{L},i}\right] \tag{4}$$

where $\mathrm{KAM}_{\mathrm{L},i}$ represents the local LocMis value at

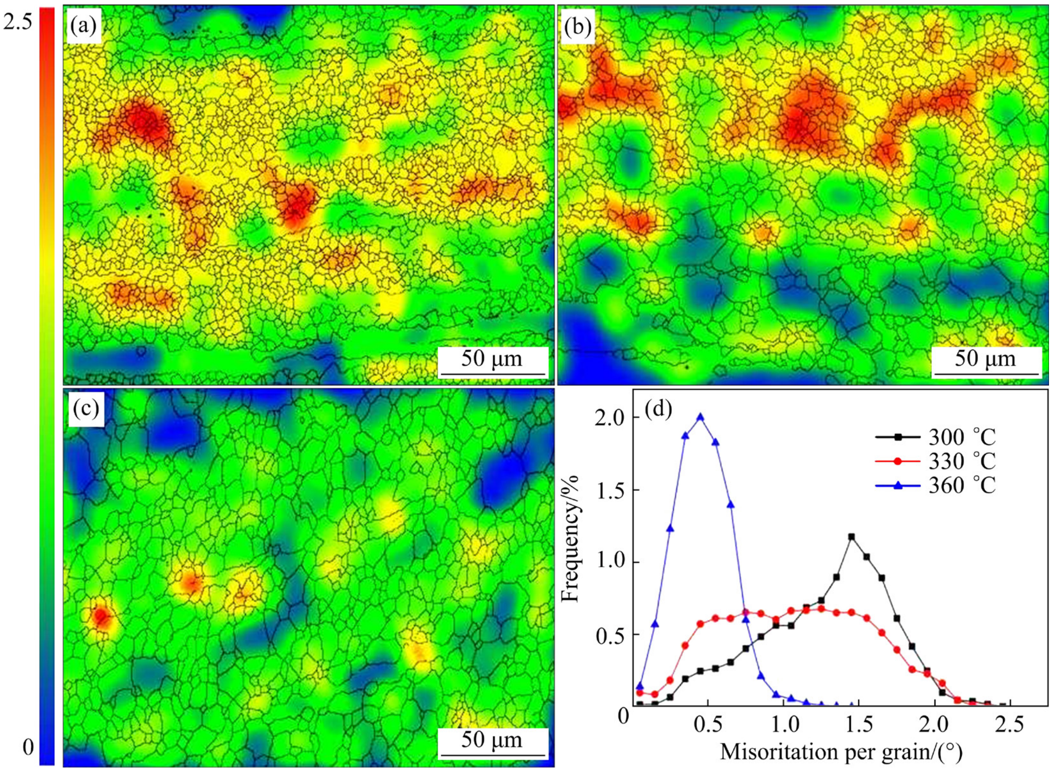

Fig. 8 EBSD stress contour maps (a, b, c) and stress contour statistic curves (d) of as-extruded alloy at different extrusion temperatures: (a) 300 °C; (b) 330 °C; (c) 360 °C

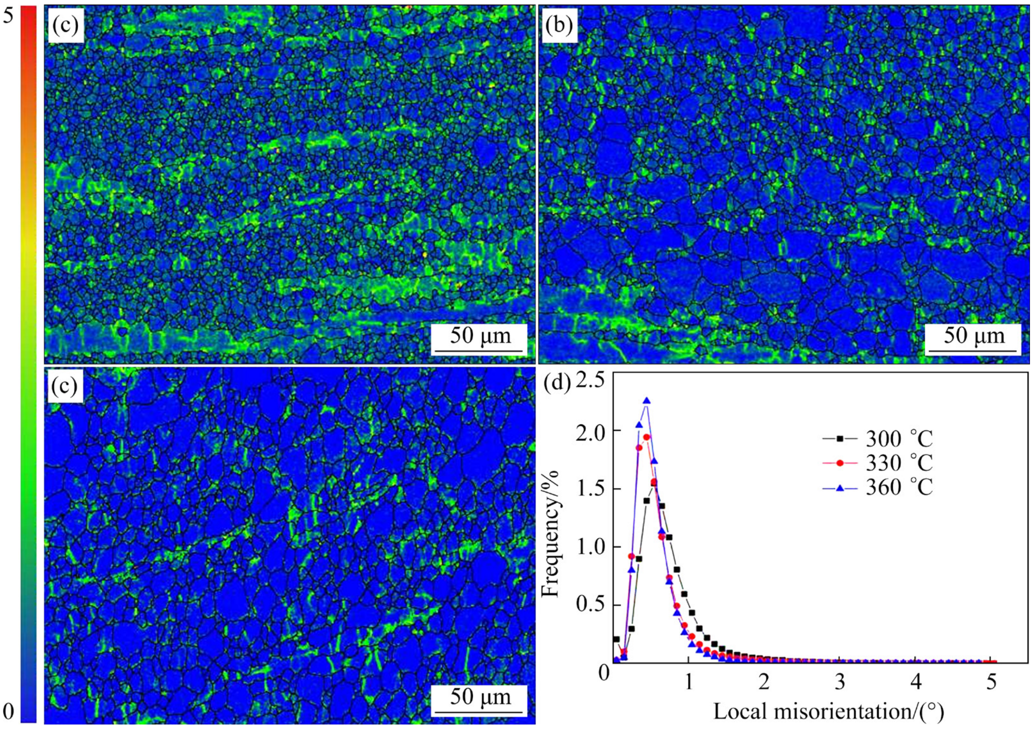

Fig. 9 KAM graphs (a−c) and KAM value statistic chart (d): (a) 300 °C; (b) 330 °C; (c) 360 °C

Point *i*, and *N* denotes the number of points in the test area. Figure 9(d) indicated that average LocMis value relationship was $\mathrm{LocMis_{av}}$ at 300 °C > $\mathrm{LocMis_{av}}$ at 330 °C > $\mathrm{LocMis_{av}}$ at 360 °C, the dislocation density tended to decrease with the increase in the temperature. Dislocation density decreased when the grain boundary swept through these high-density dislocation regions, and crystal grains grew up.

Figure 4 showed that the small-angle grain was composed of high-density dislocations, and its boundary was mainly concentrated in un-DRXed grains. Dislocation tangles appeared with increasing the dislocation density, thus forming green cell-like substructures (Figs. 4(a, b)). At the extrusion temperature of 300 °C, DRX at the DRXed grains was mainly CDRX which increased dislocations-formed sub-grain boundaries. Subsequently, the sub-grain boundaries continued to absorb dislocation. Finally, a low-angle grain boundary converted into a high-angle grain boundary, and the sub-crystal converted into a real grain. Since this process did not involve the migration of high-angle grain boundaries, this dynamic recrystallization was termed CDRX. Moreover, the research of HE et al [27] showed that DRV could offset most of the first type residual stress and a small part of the second type residual stress, while DRX can not only offset most of the first type residual stress, but also offset most of the second type residual stress. Thus, the difference ($\sigma_1-\sigma_2$) in Fig. 6(b) increased when the extrusion temperature increased. In addition, both the KAM diagram and LocMis show that there were high-density dislocations in un-DRXed area, which indicates that DRV dominates in the un-DRXed grains. Likewise, the increase of the average grain size and the disappearance of small-angle grain boundaries were completed by the migration of large-angle grain boundaries at an extrusion temperature of 360 °C, which also belonged to DDRX.

4.2 Effect of extrusion temperature on deformation mechanism

The plastic deformation of magnesium alloy always starts the basal slip at ambient temperature, but the basal slip has only two independent slip systems [27]. The von Mises yield criterion highlights that only 5 independent slip systems simultaneously participating in the deformation, can enter into yield phase during plastic deformation. Accordingly, the plastic deformation of magnesium alloy often starts the twinning deformation mechanism to make up for the lack of slip systems [27]. The critical shear stress (τ_{CRSS}) on the non-basal sliding surface decreased with increasing the deformation temperature, so the non-basal sliding system started, which improved the deformation ability at high temperatures [30]. According to the NAN et al's research [23], the critical shear stress on the prismatic slip was several magnitude orders larger than that of the basal slip. According to Schmid's law, the minimum cutting stress (σ_0) of the sliding system in the single crystal can be expressed as [2]

$$\sigma_0=\tau_{\mathrm{CRSS}}/m_{\mathrm{s}} \tag{5}$$

The non-basal plane slip system is difficult to start at ambient temperature. In this study, the τ_{CRSS} on $\{10\bar{1}0\}$ and $\{11\bar{2}0\}$ prismatic planes decreased with increasing the extrusion temperature. On the other hand, the m_{s} on two prismatic planes was higher than that on the basal plane, so the contribution of $\{10\bar{1}0\}$ and $\{11\bar{2}0\}$ prismatic planes to the plastic deformation increased, thus enhancing the texture intensity on both $\{10\bar{1}0\}$ and $\{11\bar{2}0\}$ prismatic planes. It was noteworthy that although the m_{s} value on the prismatic $\{10\bar{1}0\}$ plane was not very different from that of prismatic $\{11\bar{2}0\}$ plane, the texture strength on the prismatic $\{10\bar{1}0\}$ plane was higher than that on the prismatic $\{11\bar{2}0\}$ plane, since the τ_{CRSS} on the $\{11\bar{2}0\}$ prismatic plane was higher than that on the $\{10\bar{1}0\}$ prismatic plane. Moreover, the magnesium alloy would start the pyramidal slip system at higher temperatures, especially the $\langle c+a\rangle$ pyramidal slip ($\{11\bar{2}2\}\langle 11\bar{2}3\rangle$) had five independent slips, their independent slipping could meet the von Mises yield criterion, thus greatly improving the alloy plastic deformation ability at high temperatures [31].

4.3 Contribution of different strengthening mechanisms to mechanical properties of as-extruded alloy

The comprehensive mechanical properties of 330 °C as-extruded alloy was optimal, the improvement of mechanical properties was due to the following four aspects.

(1) Grain refinement strengthening

In order to quantitatively analyze the fine crystal strengthening effect ($\Delta\sigma_{\mathrm{S}}$), we applied the Hall−Page formula:

$$\Delta\sigma_{\mathrm{S}}=K(d_2^{-1/2}-d_1^{-1/2}) \tag{6}$$

where K is a constant and K=0.08 MPa·m$^{1/2}$, d_1 and

d_2 represent the average grain sizes of the as-cast and as-extruded alloys (330 °C), respectively, and fine grain strengthening contribution was 45.7 MPa after calculation.

(2) Particle strengthening

The quasi-crystal I phase was crushed into fine particles during extrusion, and dispersed into α-Mg matrix, thus playing a strengthening role by inhibiting the dislocations movement [31]. There were indeed quasi-crystal I phase particles with a size of nearly 1 μm at the bottom of the dimple. The relationship between size and strengthening effect of the second phase particles ($\Delta\sigma_{\mathrm{Orowan}}$) can be expressed as [32]

$$\Delta\sigma_{\mathrm{Orowan}} = \frac{0.13G_{\mathrm{m}}b}{\lambda}\ln\frac{d}{2b} \tag{7}$$

$$\lambda \approx d\left[\left(\frac{1}{2V_{\mathrm{p},I}}\right)^{1/3}-1\right] \tag{8}$$

where G_{m} denotes the magnesium alloy shear modulus, λ is the distance between second phase particles, d represents average size of the quasi-crystal I phase particle, and $V_{\mathrm{p},I}$ describes the volume fraction of the I phase particle (the volume fraction was obtained from the second phase of the as-cast alloy). The contribution of the Orowan strengthening to as-extruded alloy was 25.3 MPa after calculation.

(3) Load-bearing strengthening

The load-bearing strengthening mechanism was closely related to the second phase. Orowan strengthening was suitable for relatively small second phase particles, whereas Fig. 2 showed that some larger quasi-crystal I phases undergoing extrusion were distributed in cluster. The mechanical properties between quasi-crystal I phase and α-Mg matrix were of great difference [32]. As shown in Fig. 10, the maximum penetration depths of the second phase and matrix were 283 nm and 415 nm, respectively. The modulus and hardness of quasi-crystal I phase were higher than those of α-Mg matrix, implying large difference in ductility between them. According to the shear-lag theory, the stress will increase due to different ductilities between the α-Mg matrix and the quasi-crystal I phase when the shear stress is transferred at the interface between them, which can be expressed as [33]

$$\sigma_{\mathrm{Load}} = \sigma_{\mathrm{m}}\left[\frac{V_{\mathrm{p}}(s+2)}{2}+V_{\mathrm{m}}\right] \tag{9}$$

where σ_{Load} is the stress caused by load transfer, V_{p} and V_{m} denote the volume fractions of the strengthened phase particles and α-Mg matrix, respectively, σ_{m} represents the yield strength of as-extruded alloy, and s is the aspect ratio. The $s\approx 1$ for the quasi-crystal I phase, since $V_{\mathrm{p}}+V_{\mathrm{m}}=1$, the load-bearing strengthening ($\Delta\sigma_{\mathrm{Load}}$) mechanism can be expressed as

$$\Delta\sigma_{\mathrm{Load}} = \frac{1}{2}V_{\mathrm{p}}\sigma_{\mathrm{m}} \tag{10}$$

The contribution of the load-bearing strengthening mechanism to as-extruded alloy was 10.2 MPa after calculation.

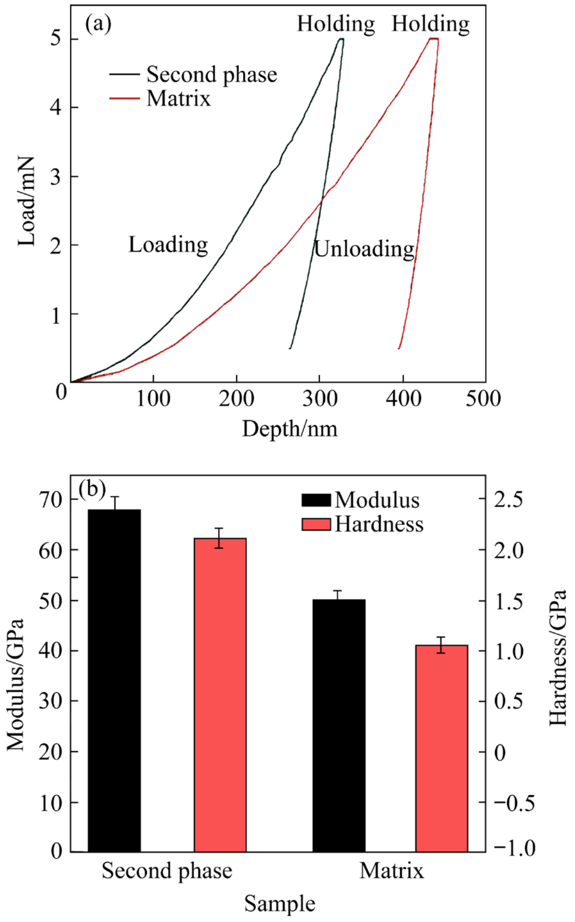

Fig. 10 Load−depth curves (a) and corresponding elastic modulus and hardness (b) for quasi-crystal I phase and matrix of as-extruded alloy at 330 °C

(4) Dislocation strengthening (work hardening)

Since the DRX proportion does not reach 100%, dislocation strengthening would play a significant role in improving the as-extruded alloy strength. A considerable amount of residual stress in the as-extruded alloy together with geometric dislocation density ρ^{GND} revealed that remaining work hardening significantly affected the alloy strength. Here, the contribution of work hardening is defined as $\Delta\sigma_{\mathrm{D}}$:

$$\Delta\sigma_{\mathrm{D}}=\sigma_{\mathrm{m}}-\Delta\sigma_{\mathrm{Load}}-\Delta\sigma_{\mathrm{Orowan}}-\Delta\sigma_{\mathrm{S}}=45.8\ \mathrm{MPa} \tag{11}$$

Based on the above calculations, Fig. 11 shows the contribution of various strengthening mechanisms to the as-extruded alloy strength.

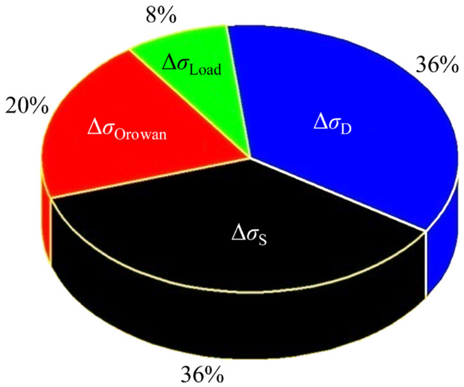

Fig. 11 Contribution of different strengthening mechanisms to strength of as-extruded alloy at 330 °C

4.4 Hot extrusion effect on fracture mechanism

Figure 12 shows the fracture morphologies of the as-cast and as extruded alloys. Figure 12(a) illustrates the fracture morphology of the as-cast alloy. The fracture morphology was composed of a large number of dimples. The particles appearing at the bottom of dimple were detected as quasi-crystal *I* phase. The oval shearing dimples in Fig. 12(a) indicated that shear stress plays a major role in the

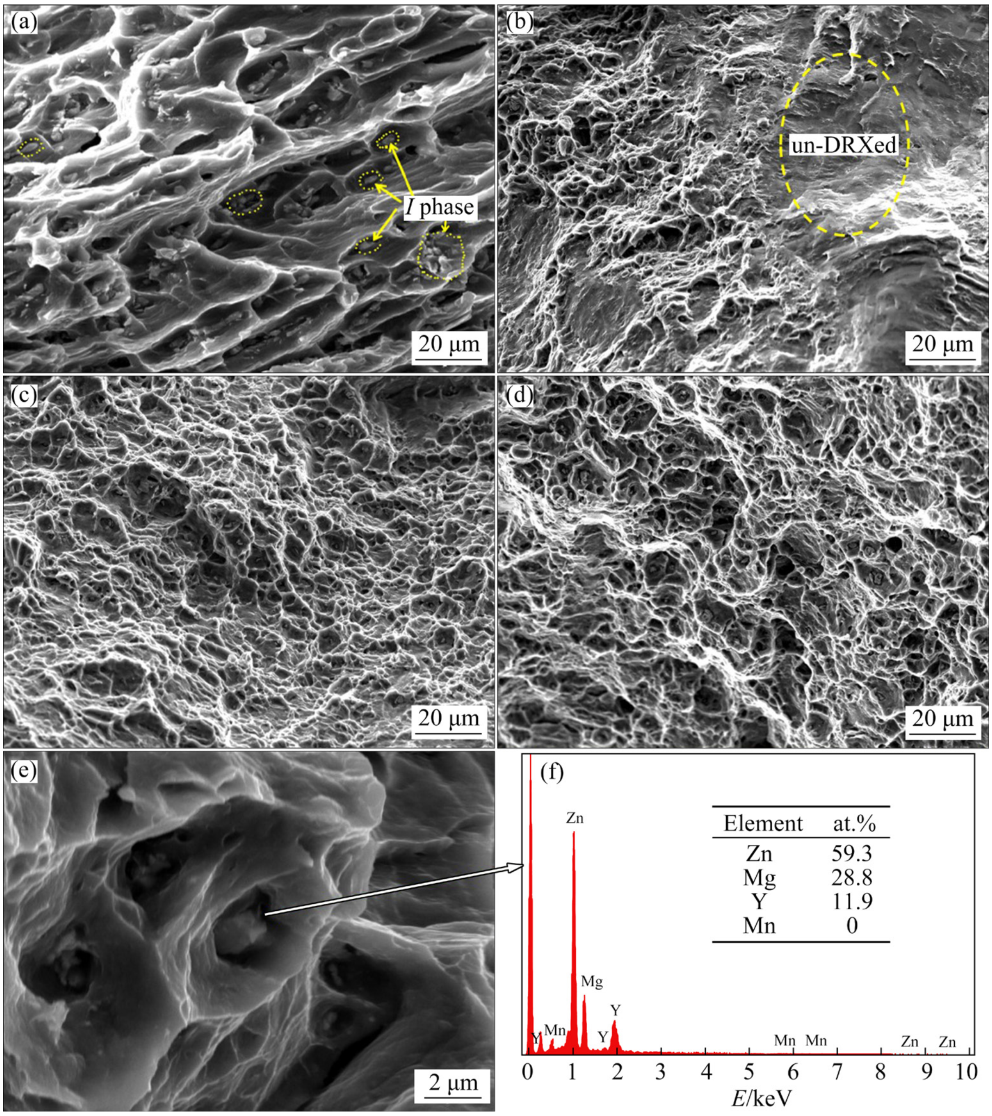

Element	at.%
Zn	59.3
Mg	28.8
Y	11.9
Mn	0

Fig. 12 Fracture morphologies of as-cast (a) and as-extruded (b−e) alloys: (a) As-cast; (b) 300 °C; (c) 330 °C; (d) 360 °C; (e) High-resolution dimple at 360 °C; (f) EDS results of second phase at bottom of dimple

fracture process [34,35]. The shear stress reached the maximum value on the inclined plane at 45° to the stretching axis during stretching process，so the cutting stress reached the maximum when the sliding surface and the sliding direction were 45° to the applied stress. Finally, slipping occurs when the cutting stress reaches the critical cutting stress [36].

The normal stress σ_α is perpendicular to the oblique section and the shear stress τ_α is tangential to the oblique section, as shown in Fig. 13. The relationship between σ_α, τ_α and α can be expressed as [37]

$$\sigma_\alpha=P_\alpha\cos\alpha=\sigma\cos^2\alpha \tag{12}$$

$$\tau_\alpha=P_\alpha\sin\alpha=\frac{\sigma}{2}\sin(2\alpha) \tag{13}$$

where σ is the normal stress, P_α is the stress on the fracture surface, and α is the intersection angle between σ_α and σ.

Figure 12(a) showed that the dimples of the as-cast alloy were elongated, and the axis of the dimples had a certain angle α with the applied tensile stress. The normal stress σ_α reached the maximum when α=0°, so the dimples were equiaxed dimples in Fig. 12(e). The larger the α value is, the larger the shear stress τ_α on the inclined section will be. The shear stress τ_α reached the maximum when α=45°. Under the action of shear stress, the axis of the dimples had an angle with the applied tensile stress, which caused that the dimples are oval or elongated. Furthermore, the appearance of shearing dimples also indirectly implied high ductility of the as-cast alloy.

DRX proportion was only 62.5% at the extrusion temperature of 300 °C, whereas the intensity of texture reached 17.14. Thus, all un-DRXed grains were so coordinated that they could be considered to be large grains, which had a large orientation difference with the surrounding DRXed grains and were difficult to coordinate deformation with surrounding DRXed grains [38]. The “hard grain” had less hindrance to the crack, so the crack would be easy to propagate and split along a specific crystal plane to form the “river-like” pattern, as shown in Fig. 12(b). Those specific crystal planes are termed as cleavage planes with large interplanar spacing, weak bonding and easily formed crack. The cleavage plane of magnesium alloy with the hcp crystal structure was usually the base plane {0001} [6,35]. When the extrusion temperature was 330 °C, the “river-like” pattern was reduced as compared with that at 300 °C, and it was replaced by a large number of equiaxed dimples. The equiaxed dimples at 330 and 360 °C were different from the shearing dimple of as-cast alloy, and the equiaxed dimple axis was basically consistent with the direction of the fracture surface, indicating that the failure of the material is mainly caused by normal stress instead of shear stress [39]. However, some local partial tearing edges also exhibited brittle fracture. The fracture morphology was basically composed of equiaxed dimples at 360 °C. In addition, some granular quasi-crystal *I* phase shown in Fig. 12(e) could be clearly observed at the bottom of the dimples. The EDS analysis of Fig. 12(f) confirmed that the composition of above granular second phase was close to that of the quasi-crystal *I* phase. Thus, a conclusion can be drawn that the fracture failure of the as-extruded alloy at higher temperatures was similar to that of the as-cast alloy. The originating cracked near the second phase generated stress concentration between the magnesium matrix and the second phase, thus causing the interface to open and form smicropores, then the enlargement and connection of the micropores to form a dimple [40]. The only difference was that as-cast alloy dimples were mostly shearing dimples, while the dimples of as-extruded alloys were equiaxed. To be specific, the as-cast alloy was sheared off during the stretching process while the as-extruded alloy was pulled off.

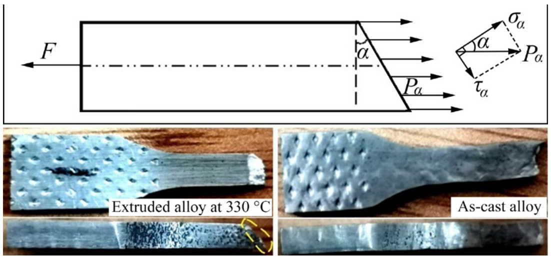

Fig. 13 Stress distribution on fracture surfaces of as-cast and as-extruded alloys (*F* is the applied load)

5 Conclusions

(1) The structure of the as-cast alloy was significantly refined after hot extrusion since the DRX, DRV and CDRX occurred simultaneously in the deformed microstructure at the extrusion

temperature of 300 °C. The above process primarily involved the dislocation forming, dislocation tangles and cellular substructures. At the extrusion temperature of 330 and 360 °C, the deformation was dominated by DDRX, which involved the migration of high-angle grain boundaries and reduced dislocation density.

(2) The $\{10\bar{1}0\}$ prismatic type I and $\{0001\}$ basal plane primarily contributed to the plastic deformation, whereas the m_s on $\{11\bar{2}0\}$ prismatic type II slip tended to increase with increasing the extrusion temperature.

(3) Hot extrusion also changed the fracture mechanism of the as-cast alloy. The fracture mode changed from ductile fracture, in which shear stress played a leading role in ductile fracture with normal stress as the main role, to the normal stress as the main role.

(4) The strength strengthening is not the generally accepted single fine-grain strengthening, whereas it is caused by multiple factors. The contribution of the fine grain strengthening, dislocation strengthening, second phase particle-induced Orowan strengthening and load-bearing strengthening to the strength of the as-extruded alloy (330 °C) accounts for 36%, 36%, 20% and 8%, respectively.

Acknowledgments

This work was financially supported by the National Nature Science Foundation of China (Nos. 51574175, 51474153).

References

[1] HU Guang-shan, ZHANG Ding-fei, TANG Tian, JIANG Lu-yao, PAN Fu-sheng. Effect of extrusion temperatures on microstructures and mechanical properties of Mg−6Zn−1Mn−4Sn−0.5Y alloy [J]. Rare Metal Materials and Engineering, 2016, 45(5): 1111−1116.

[2] WANG Bo-ning, WANG Feng, WANG Zhi, LIU Zheng, MAO Ping-li. Fabrication of fine-grained, high strength and toughness Mg alloy by extrusion shearing process [J]. Transactions of Nonferrous Metals Society of China, 2021, 31(3): 666−678.

[3] TONG Li-bo, ZHENG Ming-yi, CHENG Li-ren, KAMADO S, ZHANG Hong-jian. Effect of extrusion ratio on microstructure texture and mechanical properties of indirectly extruded Mg−Zn−Ca alloy [J]. Materials Science and Engineering A, 2013, 569: 48−53.

[4] XU S W, MATSUMOTO N, KAMADO S, HOMMA T, KOJIMA Y. Effect of homogenization on microstructures and mechanical properties of hot compressed Mg−9Al−lZn alloy [J]. Materials Science and Engineering A, 2011, 528: 2385−2393.

[5] SHI Lai-xin, LI Hu, LV Hu-yuan, LI Min-gao, ZHOU Tao, YANG Ming-bo. Microstructure and texture evolution of AZ31 magnesium alloy thin sheet processed by hot rolling−shearing−bending [J]. Metals and Materials International, 2022, 28(5): 1224−1231.

[6] XU C, NAKATA T, QIAO X G, JIANG H S, SUN W T, CHI Y C, ZHENG M Y, KAMADO S. Effect of extrusion parameters on microstructure and mechanical properties of Mg−7.5Gd−2.5Y−3.5Zn−0.9Ca−0.4Zr (wt.%) alloy [J]. Materials Science and Engineering A, 2017, 685: 159−167.

[7] MORIKAWA T, KINOSHITA D, KAWAMURA Y, HIGASHIDA K. Fine-grained structure in extruded magnesium alloy with long-period stacking order phase [J]. Materials Science Forum, 2007, 561: 905−908.

[8] FAN Yang, YIN Shu-ming, LI Shou-xin, ZHANG Zhe-feng. Crack initiation mechanism of extruded AZ31 magnesium alloy in the very high cycle fatigue regime [J]. Materials Science and Engineering A, 2008, 491): 131−136.

[9] DING Han-li, LIU Liu-fa, KAMADO S, DING Wen-jiang, KOJIMA Y. Study of the microstructure, texture and tensile properties of as-extruded AZ91 magnesium alloy [J]. Journal of Alloys and Compounds, 2008, 456(1/2): 400−406.

[10] WU Xiao-feng, XU Chun-xiang, ZHANG Zheng-wei, YANG Wen-fu, ZHANG Jin-shan, ZHANG Wen-xin. Effect of Y-element on microstructure and mechanical properties of as-cast Mg−3Zn−1Mn alloy containing *I* and *W* phase [J]. Advanced Engineering Materials, 2020, 22: 1900964.

[11] ANBUSELVAN S, RAMANATHAN S. Hot deformation and processing maps of extruded ZE41A magnesium alloy [J]. Materials & Design, 2010, 31(5): 2319−2323.

[12] ZENG Rong-chang, HAN En-hou, KE Wei, DIETZEL W, KAINER K U, ATRENS A. Influence of microstructure on tensile properties and fatigue crack growth in extruded magnesium alloy AM60 [J]. International Journal of Fatigue, 2010, 32(2): 411−419.

[13] SARKER D, CHEN Dao-lun. Texture transformation in an extruded magnesium alloy under pressure [J]. Materials Science and Engineering A, 2013, 582: 63−67.

[14] MIRZA F A, CHEN Dao-lun, LI De-jiang, ZENG Xiao-qin. Effect of strain ratio on cyclic deformation behavior of a rare-earth containing extruded magnesium alloy [J]. Materials Science and Engineering A, 2013, 588: 250−259.

[15] LIU Ying, CHEN Wei-ping, ZHANG Wei-wen. Effects of RE on microstructures and mechanical properties of hot-extruded AZ31 magnesium alloy [J]. Journal of Rare Earth (English Edition), 2004(4): 527−532.

[16] SRINIVASAN M, LOGANATHAN C, NARAYANASAMY R, SENTHILKUMAR V S, NGUYEN Q B, GUPTA M. Study on hot deformation behavior and microstructure evolution of cast-extruded AZ31B magnesium alloy and nanocomposite using processing map [J]. Materials & Design, 2013, 47: 449−455.

[17] YU Kun, RUI Shou-tai, WANG Xiao-yan, WANG Ri-chu, LI Wen-xian. Texture evolution of extruded AZ31 magnesium alloy sheets [J]. Transactions of Nonferrous Metals Society of China, 2009, 19: 511−516.

[18] LI Hui-zhong, WEI Xiao-yan, OUYANG Jie, JIANG Jun, LI Yi. Hot deformation behavior of extruded AZ80 magnesium alloy [J]. Transactions of Nonferrous Metals Society of China, 2013, 23(11): 3180−3185.

[19] ZHANG Jing, LI Wei-guo, GUO Zheng-xiao. Static recrystallization and grain growth during annealing of an extruded Mg−Zn−Zr−Er magnesium alloy [J]. Journal of Magnesium and Alloys, 2013, 1(1): 31−38.

[20] LIU Tian-mo, LIU Jian-zhong, LU Li-wei, HQ Yuan, SHI Xiu-Ling, PAN Fu-sheng. Microstructure and deformation behavior of dual-directional extruded AZ31 magnesium alloy [J]. The Chinese Journal of Nonferrous Metals, 2010, 20(9): 1657−1664. (in Chinese)

[21] BARNETT M R. Taylor model based description of the proof stress of magnesium AZ31 during hot working [J]. Metallurgical and Materials Transactions A, 2003, 34: 1799−1806.

[22] SARKER D, FRIEDMAN J, CHEN D L. Twin growth and texture evolution in an extruded AM30 magnesium alloy during compression [J]. Journal of Materials Science & Technology, 2014, 30(9): 884−887.

[23] NAN Xiao-long, WANG Hui-yan, ZHANG Lei, LI Jin-biao, JIANG Qin-chuan. Calculation of Schmid factors in magnesium: Analysis of deformation behaviors [J]. Scripta Materialia, 2012, 67(5): 443−446.

[24] LIU Xiao, JONAS J J, LI Luo-xing, ZHU Bi-wu. Flow softening, twinning and dynamic recrystallization in AZ31 magnesium [J]. Materials Science and Engineering, 2013, 583: 242−253.

[25] JIANG Ting, GUO Xue-feng, MA Guang. Microstructures and properties of reciprocating extruded as-cast ZK60 magnesium alloy [J]. Transactions of Nonferrous Metals Society of China, 2007, 17(s1): 396−399.

[26] WONG T W, HADADZADEH A, WELLS M A. High temperature deformation behavior of extruded AZ31B magnesium alloy [J]. Journal of Materials Processing Technology, 2018, 251: 360−368.

[27] HE Wei-wei, ZHANG Kun, HUANG Min, DAI Sheng-long. Influence of secondary phases on dynamic recrystallization mechanisms in extruded Mg−Zn−Y magnesium alloy [J]. Journal of Aeronautical Materials, 2012, 32(5): 7−17.

[28] WANG Wen, HAN Peng, PENG Pai, GUO Hong-ju, HUANG Li-ying, QIAO Ke, HAI Min-na, YANG Qi, WANG Hong-duo, WANG Kuai-she, WANG Li-qiang. Superplastic deformation behavior of fine-grained AZ80 magnesium alloy prepared by friction stir processing [J]. Journal of Materials Research and Technology, 2020, 9(3): 5252−5263.

[29] YAN Zhi-feng, WANG Deng-hui, HE Xiu-li, WANG Wen-xian, ZHANG Hong-xia, DONG Peng, LI Chen-hao, LI Yu-li, ZHOU Jun, LIU Zhuang, SUN Li-yong. Deformation behaviors and cyclic strength assessment of AZ31B magnesium alloy based on steady ratcheting effect [J]. Materials Science & Engineering A, 2018, 723(18): 212−220.

[30] WANG Guan-gang, HUANG Guang-sheng, CHEN Xiang, DENG Qian-yuan, TANG Ai-tao, JIANG Bin, PAN Fu-sheng. Effects of Zn addition on the mechanical properties and texture of extruded Mg−Zn−Ca−Ce magnesium alloy sheets [J]. Materials Science and Engineering A, 2017, 705: 46−54.

[31] TONG Li-bo, ZHENG Mi-yi, CHENG Li-ren, ZHANG De-ping, KAMADO S, MENG Jian, ZHANG Hong-jie. Influence of deformation rate on microstructure, texture and mechanical properties of indirect-extruded Mg−Zn−Ca alloy [J]. Materials Characterization, 2015, 104: 66−72.

[32] YU Zhao-peng, YAN Yu-hao, YAO Jia, WANG Cheng, ZHA Min, XU Xin-yu, LIU Yan, WANG Hui-yuan, JIANG Qi-chuan. Effect of tensile direction on mechanical properties and microstructural evolutions of rolled Mg−Al−Zn−Sn magnesium alloy sheets at room and elevated temperatures [J]. Journal of Alloys and Compounds, 2018, 744: 211−219.

[33] SUN Wang-ting, XU Chao, QIAO Xiao-guang, ZHENG Ming-yi, KAMADO S, GAO Nong, STARINK M J. Evolution of microstructure and mechanical properties of an as-cast Mg−8.2Gd−3.8Y−1.0Zn−0.4Zr alloy processed by high pressure torsion [J]. Materials Science and Engineering A, 2017, 700: 312−320.

[34] WU Bo-lin, ZHAO Yu-hua, DU Xing-hao, ZHANG Yu-dong, WAGNER F, ESLING C. Ductility enhancement of extruded magnesium via yttrium addition [J]. Materials Science and Engineering A, 2010, 527: 4334−4340.

[35] WANG Wen-ke, CHEN Wen-zhen, ZHANG Wen-cong, CUI Guo-rong, WANG Er-de. Weakened anisotropy of mechanical properties in rolled ZK60 magnesium alloy sheets with elevated deformation temperature [J]. Journal of Materials Science & Technology, 2018, 34(11): 2042−2050.

[36] TAHREEN N, ZHANG Ding-fei, PAN Fu-sheng, JIANG Xian-quan, LI Dong-yang, CHEN Dao-lun. Strengthening mechanisms in magnesium alloys containing ternary W and LPSO phases [J]. Journal of Materials Science & Technology, 2018, 34(7): 1110−1118.

[37] ZHANG Ming-yi, QIAO Xiao-guang, XU Shi-wei, GAN Wei-ming, WU Kun, KAMADO S, KOJIMA Y, BROKMEIER H G. Effect of hot extrusion on microstructure and mechanical properties of quasicrystal-reinforced Mg−Zn−Y alloy [J]. Transactions of Nonferrous Metals Society of China, 2005, 15(4): 715−721.

[38] WU Qiong, ZHU Shi-jie, WANG Li-guo, LIU Qian, YUE Gao-chao, WANG Jun, GUAN Shao-kang. The microstructure and properties of cyclic extrusion compression treated Mg−Zn−Y−Nd alloy for vascular stent application [J]. Journal of the Mechanical Behavior of Biomedical Materials, 2012, 8(2): 1−7.

[39] ZHANG Bao-ping, WANG Yin, GENG Lin, LU Chun-xiang. Effects of calcium on texture and mechanical properties of hot-extruded Mg−Zn−Ca alloys [J]. Materials Science and Engineering A, 2012, 539: 56−60.

[40] ZHANG Ding-fei, QI Fu-gang, LAN Wei, SHI Guo-liang, ZHAO Xia-bing. Effects of Ce addition on microstructure and mechanical properties of Mg−6Zn−1Mn alloy [J]. Transactions of Nonferrous Metals Society of China, 2011, 21(4): 703−710.

高塑性 Mg−3Zn−1Y−1Mn 合金在不同挤压温度下的组织演变、强化机制和变形行为

武晓峰，许春香，张正卫，杨文甫，张金山

太原理工大学 材料科学与工程学院，太原 030024

摘　要：为了改善铸态 Mg−3Zn−1Y−1Mn 合金的力学性能、研究合金在不同变形温度下的组织演变规律和变形机理，对铸态 Mg−3Zn−1Y−1Mn 合金进行热挤压实验。实验结果显示，当挤压温度为 330 ℃时，挤压态合金具有最佳的力学性能，抗拉强度和伸长率分别达到 270 MPa 和 16.8%。挤压态合金性能大幅提高主要归因于 3 个方面：由动态再结晶导致的细晶强化作用、未被动态再结晶抵消的加工硬化以及第二相粒子强化作用。在热挤压过程中，当挤压温度为 300 ℃时，同时发生连续动态再结晶和动态回复；而当挤压温度为 330 和 360 ℃时，发生不连续动态再结晶。此外，在热变形过程中$\{0001\}$基面滑移、$\{10\bar{1}0\}$ I 型柱面滑移和$\{11\bar{2}0\}$ II 型柱面滑移对塑性变形的贡献受挤压温度影响很大，而$\{11\bar{2}0\}$ II 型柱面是 3 个滑移系中最难启动的滑移系。

关键词：Mg−3Zn−1Y−1Mn 合金；显微组织；变形机制；热挤压；动态再结晶；力学性能

(Edited by Wei-ping CHEN)